

# Fast X-ray Phase-Contrast Imaging of Electrospinning Polymer Jets: Measurements of Radius, Velocity, and Concentration

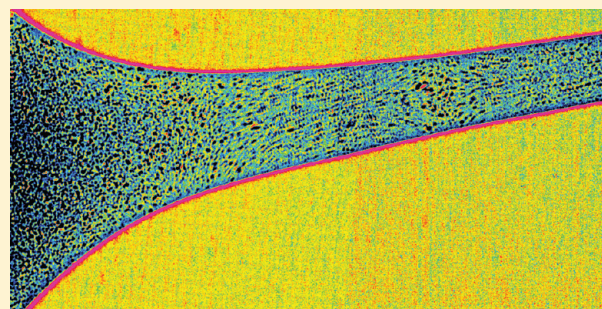
Israel Greenfeld,<sup>\*,†</sup> Kamel Fezzaa,<sup>‡</sup> Miriam H. Rafailovich,<sup>§</sup> and Eyal Zussman<sup>†</sup>

<sup>†</sup>Department of Mechanical Engineering, Technion - Israel Institute of Technology, Haifa 32000, Israel

<sup>‡</sup>Advanced Photon Source, Argonne National Laboratory, Argonne, Illinois 60439, United States

<sup>§</sup>Department of Materials Science and Engineering, State University of New York, Stony Brook, New York 11794-2275, United States

**ABSTRACT:** The study of electrospinning polymer solution jets, and the evolution of the polymer entangled network during electrospinning, is of interest for understanding of the microstructure of the resulting nanofibers. Fast X-ray phase-contrast imaging was applied to investigate the flow of the first 10 mm of a straight jet of electrospinning PEO and PMMA semidilute solutions. The jet radius, velocity, and absorbance were measured at high resolution (0.67  $\mu\text{m}/\text{pixel}$ ) and at extremely short exposure time ( $<0.5 \mu\text{s}$ ), under a wide range of electrospinning conditions and solution concentrations. The flow field, measured by tracing silica microbeads, revealed laminar flow with axial velocities that implied significant mass loss due to evaporation. X-ray absorption measurements provided evidence for substantial polymer concentration rise along the jet, particularly at the jet boundaries, evidence of rapid evaporation. Furthermore, at high strain rates, the polymer concentration rose at the jet center as the velocity increased along the jet, implying polymer network lateral contraction due to axial stretching. Our findings confirm the theoretically predicted counteracting effects of evaporation and stretching on the polymer matrix within the jet.



## 1. INTRODUCTION

Electrospinning is characterized by high strain rates of the order  $10^3 \text{ s}^{-1}$ .<sup>1–7</sup> Such stretching can potentially improve the structural order within as-spun nanofibers and enhance their mechanical properties.<sup>8–12</sup> At the same time, rapid solvent evaporation during electrospinning can lead to increased polymer concentrations at the jet boundary,<sup>13–16</sup> sometimes forming a solid skin and a heterogeneous and porous structure.<sup>11,15,17</sup> Hence, study of electrospinning polymer solution jets, and specifically of the evolution of the polymer entangled network during electrospinning,<sup>11</sup> is of interest in clarifying the microstructure of as-spun nanofibers. Experimental data on the jet dynamics during the initial stage of electrospinning, and particularly on the flow regime within the jet, are needed in order to characterize the hydrodynamic environment to which the polymer network is subjected. Furthermore, data on the distribution of the polymer within the jet can shed light on the conflicting processes of stretching and evaporation for different material properties and electrospinning conditions.

The geometry and velocity of electrospinning jets were studied by optical microscopy<sup>1,5</sup> and by tracing large particles (50–70  $\mu\text{m}$ ) using high-speed visible light imaging.<sup>18</sup> Stretching and orientation of polymer chains have been observed in electrospinning jets using birefringence,<sup>19</sup> Raman,<sup>20</sup> and X-ray diffraction<sup>21</sup> techniques. Imaging of electrospinning jets using in-line fast X-ray phase-contrast imparts several advantages. The method has been used to study

flow dynamics, particularly fuel jets and sprays,<sup>22–24</sup> and offers an extremely short exposure time ( $<0.5 \mu\text{s}$ ), essential for capturing the inherently unstable electrospinning jet, and, at the same time, provides high spatial resolution (0.67  $\mu\text{m}/\text{pixel}$ ). Owing to the weak interaction of X-ray with matter, it has high penetrability, and its essentially monochromatic beam enables measurement of transmission absorption and analysis of the polymer concentration within the jet. The method also provides enhanced phase boundary contrast, enabling accurate measurement of small objects, as well as accurate velocimetry using particles as small as 1  $\mu\text{m}$ .<sup>24</sup> At the same time, the scattering of X-rays penetrating a small object is significant<sup>25</sup> and requires correction of absorption measurements.

In this work, we apply fast X-ray phase-contrast imaging toward analysis of up to 10 mm of the initial portion of electrospinning jets (the straight and stable section) to extrapolate high-resolution (0.67  $\mu\text{m}/\text{pixel}$ ) measurements of the jet radius, velocity, and absorbance. Semidilute solutions of PEO (poly(ethylene oxide)) and PMMA (poly(methyl methacrylate)) were measured under a wide range of electrospinning conditions (electric field and flow rate) and solution concentrations. The jet flow field, measured by tracing silica microbeads mixed in the polymer solutions, showed laminar flow with axial velocities that implied significant mass

Received: February 1, 2012

Revised: March 29, 2012

Published: April 10, 2012

loss due to evaporation. Absorption along and across the jet was calculated from beam transmission measurements, after correcting for the scattering effect. Substantial polymer concentration increase was observed along the jet, as early as 2–3 mm from the jet start, evidence of rapid evaporation. This concentration rise occurred particularly along the jet's boundaries. At the same time, high strain rates (e.g., due to high electric field), sufficiently distant from the orifice, led to a rise in polymer concentration at the jet center as well. This latter phenomenon is testimonial of the lateral inward contraction of the polymer network due to the axial stretching.

## 2. EXPERIMENTAL SECTION

**2.1. Equipment Setup and Operation.** The experiment was conducted at 32-ID Beamline, Advanced Photon Source (APS), Argonne National Lab, using a partially coherent undulator X-ray white beam. The experimental setup of the X-ray imaging system and the electrospinning chamber are presented in Figures 1a and 2a,b.

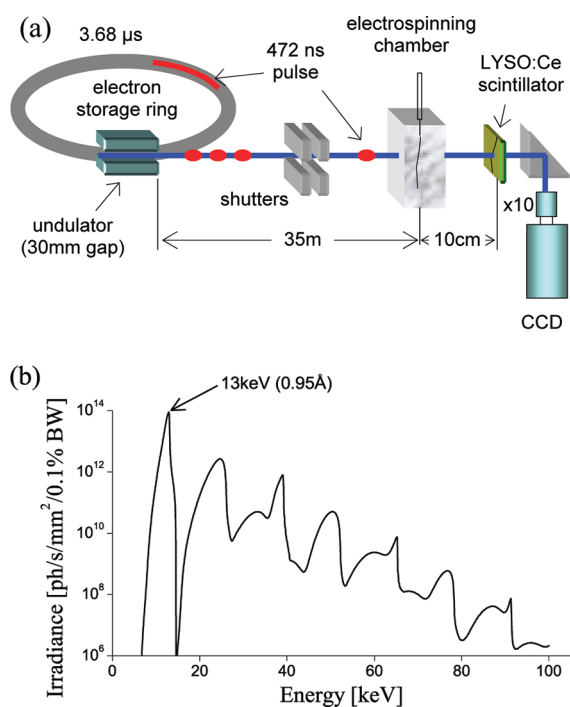


**Figure 1.** Experimental setup. (a) X-ray beam path: a millisecond shutter was set up in series with a very fast galvano-based shutter that opened the path for less than 100 μs each second. The beam penetrated the jet and was converted to a digital image via a scintillator. The CCD camera was timed to capture the first pulse after the very fast shutter opened. (b) X-ray beam flux: the dominant harmonic is indicated.

The X-ray beam was generated from the synchrotron's electron storage ring with a dominant harmonic at a beam energy of 13 keV, corresponding to a wavelength of 0.95 Å (Figure 1b). The dominant peak was ~100 times more intense than the harmonics, rendering the beam practically monochromatic, an essential feature in view of the strong dependence of material X-ray mass absorption coefficients on beam energy. The X-ray beam was emitted as short pulses, each 472 ns long, issued at intervals of 3.68 μs. A millisecond mechanical shutter opened the beam path at 1 Hz in order to protect the imaging system from overheating, and was followed by a very fast galvano-based shutter that opened the beam path for less than 100 μs each second.

The X-ray pulses penetrated the electrospinning jet, and their transmission was converted to visible light by a fast scintillator crystal (LYSO:Ce, 40 ns decay time), positioned at a distance of 10 cm from

the spinning jet. A camera, timed to capture the first pulse passing through the very fast shutter, captured the image via a folding mirror and a ×10 objective optics, using a 1280H × 1024 V CCD detector with a pixel size of 6.7 × 6.7 μm<sup>2</sup>. The beam size of 1 × 1 mm<sup>2</sup> was slightly larger than the camera's effective field-of-view. A typical X-ray image of the jet is shown in Figure 2c. Note the white corona at the jet boundaries due to edge diffraction. During particle tracing experiments, two-pulsed images were captured for each frame, separated by a time interval of 3.68 μs multiples, up to a maximum of 147.2 μs.

The electrospinning chamber (Figure 2a,b) consisted of a PMMA-based enclosure with Kapton-film windows. The chamber was mounted on a remotely controlled motorized stage, which allowed for control of *x,y,z* positioning of the electrospinning chamber, and for sequential capturing of images at 0.5 mm steps along the jet during a single session (see image example in Figure 2d). Because of the unstable nature of electrospinning jets and the small field-of-view of the camera, images could only be captured at distances of up to 10 mm from the jet start. The image frame was recorded 20 times at 1 s intervals for each stage position, with a gray scale depth of 16 bits. Dark images (no X-ray) and background images (no jet) were also collected to allow for image correction.

In order to avoid prolonged exposure of the jet to X-ray radiation that might degrade the polymer or affect the solvent, the following measures were taken. After allowing sufficient time for the jet flow to become steady, the camera was triggered to capture the first pulse released by the very fast shutter. In the absorption measurement experiments, only a single pulse was captured, and the jet was consequently exposed to the beam for 0.47 μs. In the particle tracing experiments, the beam path was left open until the second image was captured, and therefore the jet was exposed to 3–41 pulses, depending on the selected time interval, and consequently the cumulative exposure time varied between 1.4 and 19.4 μs. The corresponding fluence (time-integrated flux) of the beam spectrum shown in Figure 1b was several orders of magnitude below typical X-ray damaging fluences.<sup>26</sup> Also, owing to the beam small size, irradiation was restricted to the jet section that was currently imaged, about 1 mm long, while the rest of the jet was not exposed to the beam. Finally, the experimental evidence from the particle tracing experiments using different exposure times has shown that the measured jet radius and particles velocity were not sensitive to exposure time, implying that the beam did not influence the jet dynamics or evaporation.

**2.2. Materials and Test Cases.** PEO ( $M_w$  600 kDa) and PMMA ( $M_w$  70 kDa) were purchased from Sigma-Aldrich. PEO was dissolved in water at concentrations of 3 and 5 wt %; PMMA was dissolved in CHCl<sub>3</sub> (chloroform) at concentration of 15 wt %. Glycerol was purchased from Sigma-Aldrich. During velocimetry tests, the PEO solutions were mixed with silica (SiO<sub>2</sub>) microbeads, purchased from Polysciences Europe GmbH, at volume fraction of 0.9 vol %. The microbeads size ranged from 1 to 10 μm (98% of microbeads), with a mean size of 1.94 ± 0.76 μm (STD), measured using ImageJ. The relevant properties of the materials and solutions used in the experiment are listed in Table 1.

The polymer solutions were injected using a standard syringe pump, into a 25 gauge capillary needle (internal diameter 0.26 mm) installed on top of the electrospinning chamber, at flow rates *Q* ranging from 1 to 8 mL/h. A 20 gauge needle (internal diameter 0.6 mm) was used for the PEO 5% particle tracing experiments. The polymer solution was drawn from the capillary needle by an electric field, created by a standard high-voltage power supply, with electric potential ranging from 4 to 14 kV. The gap between the needle and the collector tip was adjusted to fall within a range of 2.5–6.5 cm (Figure 2a), resulting in a nominal electric field *E* of 0.6–4 kV/cm. The experiments were conducted at room temperature, at a relative humidity of 40%. Tests 1–17 and their conditions are presented in Figure 3.

**2.3. Particle Tracing.** Velocity measurements and characterization of the flow regime inside the electrospinning jet were achieved by X-ray particle tracing. The measurements were carried out on PEO 3% and 5% solutions, mixed with silica microbeads (tests 14–18). The microbeads provided good X-ray image contrast, with an absorption coefficient ~10 times higher than that of the PEO solutions (refer to

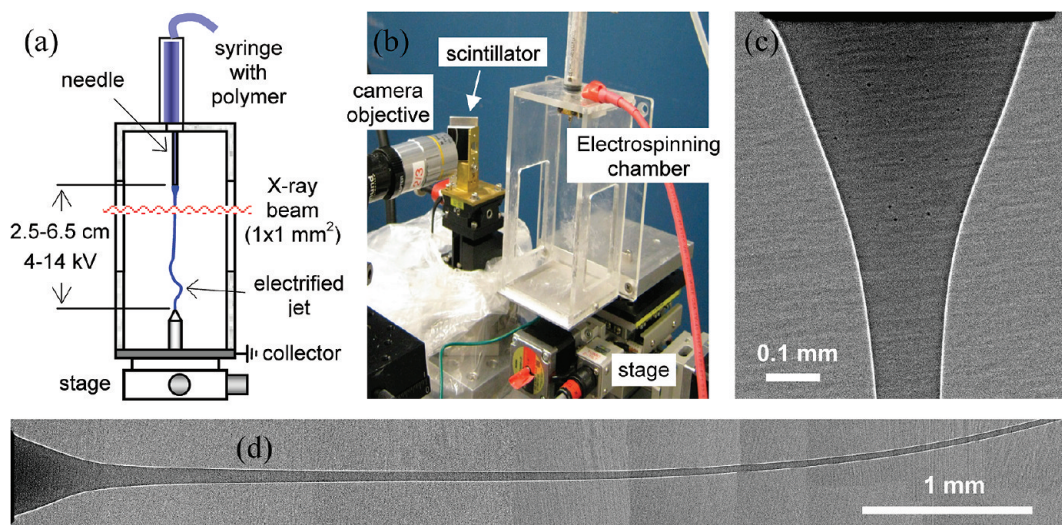


**Figure 2.** Electrospinning setup. (a) Electrospinning chamber: the polymer solution is pumped into the syringe and drawn by the electric field toward the collector. The initial rectilinear portion of the jet is imaged by sequentially moving the motorized stage upward at 0.5 mm steps. (b) Electrospinning chamber and imaging target (scintillator). (c) Representative X-ray image: electrospinning solution of 5 wt % PEO ( $M_w = 600$  kDa) in water; electric field 1.6 kV/cm, flow rate 3.2 mL/h. (d) Same test case, presenting a jet section 6 mm long, reconstructed from 12 sequential images.

**Table 1. Characteristic Properties of Tested Materials and Solutions<sup>a</sup>**

material/polymer	$M_w$ [Da]	solvent	$c$ [%]	$\mu$ [Pa s]	$\gamma$ [mN/m]	$\sigma$ [mS/m]	$\rho_p$ ( $\rho_s$ ) [g/cm <sup>3</sup> ]	$\epsilon_p$ ( $\epsilon_s$ ) <sup>b</sup> [cm <sup>2</sup> /g]	$\alpha_0$ [1/cm]
glycerol	92		100	0.9	64 <sup>c</sup>	0.006 <sup>d</sup>	1.26	1.75	2.21
PMMA	70K	chloroform	15	~0.1	28 <sup>c</sup>		1.2 (1.5)	1.45 (23.3)	28.9
PEO	600K	water	3	1.2 <sup>e</sup>	72 <sup>e</sup>	1.4 <sup>e</sup>	1.12 (1)	1.51 (2.29)	2.28
PEO	600K	water	5	12 <sup>e</sup>	75 <sup>e</sup>	1.6 <sup>e</sup>	1.12 (1)	1.51 (2.29)	2.26
silica (microbeads)							2.65	8.27	21.9

<sup>a</sup>Molecular weight  $M_w$ , concentration  $c$ , zero-shear viscosity  $\mu$ , surface tension  $\gamma$ , conductivity  $\sigma$ , mass absorption coefficient of polymer (solvent)  $\epsilon_p$  ( $\epsilon_s$ ), density of polymer (solvent)  $\rho_p$  ( $\rho_s$ ), and absorption coefficient  $\alpha_0$ . <sup>b</sup>Reference 27. <sup>c</sup>Reference 28. <sup>d</sup>SmartMeasurement. <sup>e</sup>Estimate based on Theron et al.<sup>30</sup>

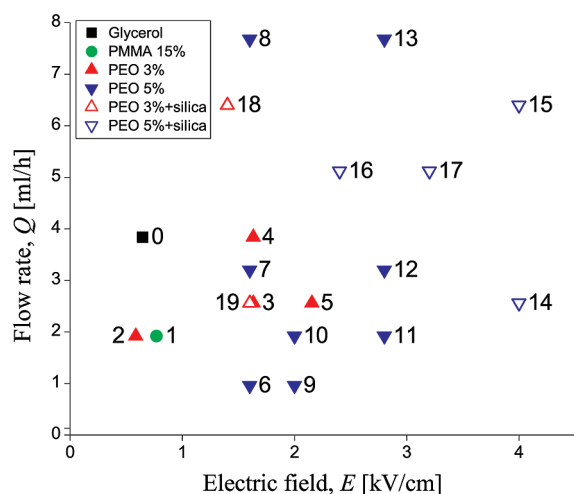


**Figure 3.** Map of X-ray tests and their respective solutions, flow rates  $Q$ , and applied electric fields  $E$ . Refer to Table 1 for corresponding material properties.

Table 1). Each jet section was exposed twice to X-ray radiation, within a short time interval, and both exposures were recorded on a single image. The time intervals used were 7.4, 18.4, 36.8, 73.6, and 147.2  $\mu$ s. Velocity vectors were calculated by tracing particles, as shown in Figure 4, and adjusting for the lateral displacement of the jet during the time interval between exposures. Typically, shorter intervals were applied in regions of high velocity, whereas longer intervals were

needed for regions of low velocity. The resulting velocity vectors were two-dimensional projections of a three-dimensional flow, but since the vertical velocity component was dominant this inaccuracy is negligible.

The small size of the particles (mean size  $\sim 2$   $\mu$ m) and their low volume fraction in the solution (0.9 vol %), as well as their homogeneous dispersion within the fluid (Figure 4), ensured minimal influence of the particles on the jet flow properties and accurate velocity measurement. Suspensions with particles volume fraction up to 1 vol % may be considered as dilute,<sup>31</sup> and therefore the effect of the particles on viscosity was negligible. Theoretical and experimental studies of the flow of particle-laden fluids in confined spaces<sup>24,32</sup> have shown that for small particles ( $d/H \leq 0.2$ , where  $d$  is the particle size and  $H$  the small dimension of the flow) and low Reynolds numbers ( $Re = \rho v D_H / \mu < O(1)$ , where  $\rho$  is the fluid density,  $v$  is the fluid velocity, and  $D_H$  is the hydraulic diameter), the particles will not cross streamlines while moving along the flow, and their velocity will be within less than 2% from the undisturbed fluid velocity. These conditions apply to the present tracing tests, where  $d < 10$   $\mu$ m,  $H \cong D_H < 1$  mm,  $\rho \cong 1$  g/cm<sup>3</sup>,  $v < 1$  m/s, and  $\mu \leq 12$  Pa s, and therefore  $d/H < 0.01$  and  $Re < 0.1$ .

The effects of particle gravity and buoyancy are negligible, in view of the high hydrodynamic forces in the electrospinning jet. The inertial force can be neglected as well (the ratio between the inertial force,  $(\pi/6)\rho_p d^3 \dot{v}$ , and the hydrodynamic force,  $3\pi\mu d v$ , acting on a particle assuming a spherical shape, is  $\rho_p d^2 s / (18\mu) \cong 10^{-6} \ll 1$ , where  $\rho_p = 2.65$  g/cm<sup>3</sup> is the particle density and  $s = \dot{v}/v < 10^3$  1/s is the flow strain rate).

**2.4. Radiation Transmission and Absorption.** Characterization of the polymer concentration distribution within the jet was achieved by measuring the X-ray transmission through the jet and calculating

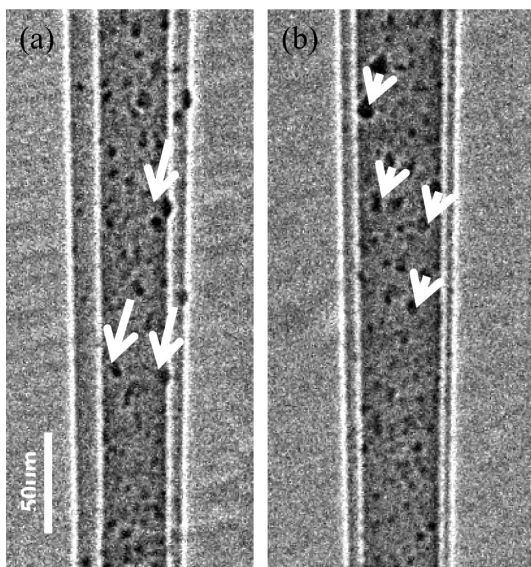


**Figure 4.** Particle tracing technique using two-pulsed X-ray images. The horizontal offset is due to the jet lateral displacement during the time interval between exposures. Representative velocity vectors (prior to correction of the lateral displacement) are indicated by arrows, correlating particles in the first image to the same particles in the second image. The solution was PEO 5% mixed with 0.9 vol % silica microbeads, electrospun under an electric field of 4 kV/cm and with a flow rate of 2.6 mL/h (test 14). The measurement was taken at distance  $z = 1.6$  mm from the jet start, with a time interval between exposures of (a)  $\Delta t = 147.2 \mu\text{s}$  and (b)  $\Delta t = 73.6 \mu\text{s}$ .

the corresponding absorption coefficient at each point. Using polymer–solvent pairs that have disparate mass absorption coefficients (refer to Table 1), the measured variations in the local absorption coefficient could be converted to polymer concentration variations.

Each raw image (see example in Figure 6a) was processed, using the recorded dark and background images, for the purpose of removing the background spatial nonuniformity and normalizing the background intensity to 1. The resulting transmission of each pixel,  $T_{\text{exp}}(r,z)$ , where  $r$  and  $z$  respectively denote the radial and axial positions of the pixel in the jet, was obtained by further adjustment for the residual local background offset. The measured transmission  $T_{\text{exp}}$  (Figure 6b) was normalized by a simulated transmission,  $T_{\text{sim}}(r,z)$  (Figure 6c), that assumed a homogeneous jet without concentration variations. Normalization provided correction for scattering effects such as dispersion and edge diffraction. Polymer macromolecular orientation as a result of stretching had a negligible effect, since X-ray is absorbed by the atoms along the beam path regardless of their bonding state.<sup>27,33</sup>

The transmission  $T_{\text{sim}}$  was calculated by a wave propagation simulation designed to account for the overall optical effects of the partially coherent beam and the test setup, by combining absorption and scattering effects. The simulation was based on the Fresnel equation, which, in the paraxial approximation,<sup>34</sup> takes the form of a convolution of the object (projected sample) and a term called propagator. The code used FFTs to calculate the convolution in reciprocal space and then inverse FFTs to retrieve the intensity in real space at the detector location. The code included the most relevant experimental parameters, such as jet geometry and energy-dependent absorption coefficients and refraction indices, as well as source size, energy spectrum, and detector point spread function.

Figure 5 depicts  $T_{\text{exp}}$  and  $T_{\text{sim}}$  at a typical cross section of the jet. Note the slight increase in the measured transmission at the jet center, with respect to the simulated transmission. Since the polymer mass absorption coefficient is lower than that of the solvent (see Table 1), absorption decreases and polymer concentration increases. Note also

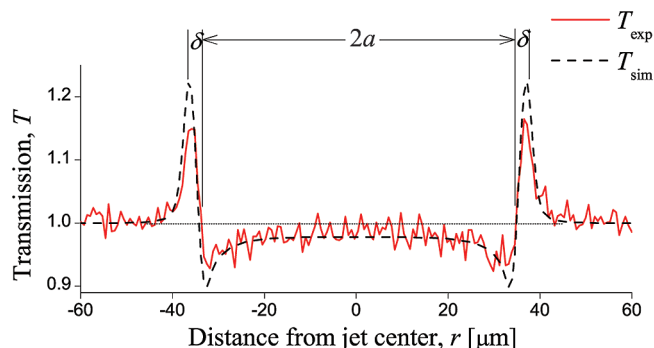


**Figure 5.** Example of the measured X-ray transmission  $T_{\text{exp}}$  at a cross section of the jet, based on test 3 (PEO 3%, 1.6 kV/cm, 2.6 mL/h) experimental data, overlaid on the simulated transmission  $T_{\text{sim}}$ . The estimated measurement error is 1.5%. The jet radius was measured at 1 pixel resolution ( $0.67 \mu\text{m}$ ) both axially and radially. The radius  $a$  was obtained by measuring the distance between the two diffraction peaks, and subtracting  $\delta = 1.5 \mu\text{m}$ , corresponding to the beam wavelength.

the increase in the measured transmission close to the jet boundary ( $r = \pm a$ ), reflecting a concentration increase near the edge as well.

Using the Beer–Lambert absorption law, and normalizing  $T_{\text{exp}}$  by  $T_{\text{sim}}$ , the average change in the apparent absorption coefficient,  $\Delta\alpha_{\text{app}}(r,z)$ , can be expressed by

$$\Delta\alpha_{\text{app}}(r, z) = -\frac{1}{d(r, z)} \ln \frac{T_{\text{exp}}(r, z)}{T_{\text{sim}}(r, z)} \quad (1)$$

where  $d(r,z) = 2a(z)(1 - [r/a(z)]^2)^{1/2}$  is the beam penetration distance at a radial position  $r$  and  $a(z)$  is the jet radius at an axial position  $z$ .<sup>11</sup> The measurement of the jet radius  $a$  was performed by detecting the edge diffraction white peaks and adjusting for a diffraction width of  $\delta = 1.5 \mu\text{m}$  corresponding to the beam wavelength (refer to Figure 5).

The measured transmission of the X-ray beam,  $T_{\text{exp}}$ , is the result of incident beam attenuation consequential of both absorption and scattering of the materials within the jet. Scattering effects of the collimated beam become significant with nonzero distances between the jet and the imaging target (the scintillator) and are relatively larger at smaller jet diameters and at regions closer to the jet boundary. Thus, the apparent absorption coefficient  $\alpha_{\text{app}}$ , obtained from pixel intensity measurements by eq 1, consists of an absorption term  $\alpha_{\text{abs}}$  and a scattering term  $\alpha_{\text{scat}}$  such that  $\alpha_{\text{app}} = \alpha_{\text{abs}} + \alpha_{\text{scat}}$ .<sup>33</sup>

In the case of a homogeneous fluid without concentration variations, the scattering contribution can be assessed by comparing the solution absorption coefficient  $\alpha_0$  to the simulated apparent absorption coefficient extrapolated from jet geometry,  $\alpha_{\text{sim}}(r,z) = -\ln T_{\text{sim}}(r,z)/d(r,z)$ . While  $\alpha_0$  accounts for absorption only,  $\alpha_{\text{sim}}(r,z)$  factors in both absorption and scattering. Assuming, as a first-order approximation, that the ratio between these two parameters is retained when concentration variations are present within the fluid, we can introduce a correction factor,  $\alpha_0/\alpha_{\text{sim}}(r,z)$ , to eq 1:

$$\Delta\alpha(r, z) \cong \frac{\alpha_0}{\alpha_{\text{sim}}(r, z)} \Delta\alpha_{\text{app}}(r, z) = \alpha_0 \left[ \frac{\ln T_{\text{exp}}(r, z)}{\ln T_{\text{sim}}(r, z)} - 1 \right] \quad (2)$$

where  $\Delta\alpha(r,z) = \alpha(r,z) - \alpha_0$  is the change in the local absorption coefficient with respect to the solution's initial absorption coefficient.

The absorption coefficient of polymer solutions is given by  $\alpha(r,z) = \epsilon_p c_p(r,z) + \epsilon_s c_s(r,z)$ ,<sup>33</sup> where  $\epsilon_p$  and  $\epsilon_s$  denote the X-ray mass absorption coefficients of the polymer and solvent and  $c_p$  and  $c_s$  denote the mass concentrations. Using the relationship  $c_s/\rho_s = 1 - c_p/\rho_p$ , the change in the local polymer concentration,  $\Delta c_p(r,z)$ , is linearly dependent on  $\Delta\alpha(r,z)$ :<sup>11</sup>

$$\Delta c_p(r, z) = c_p(r, z) - c = \frac{\Delta\alpha(r, z)\rho_p}{\varepsilon_p\rho_p - \varepsilon_s\rho_s} \quad (3)$$

where  $c$  is the solution's initial concentration and  $\rho_p$  and  $\rho_s$  are the densities of the polymer and solvent, respectively. Using  $c$  as the concentration scale, the relative concentration change may be expressed by  $\Delta c_p/c$  and the relative concentration by  $c_p/c = 1 + \Delta c_p/c$ .

The values of the parameters  $\rho_p$ ,  $\rho_s$ ,  $c$ ,  $\varepsilon_p$ ,  $\varepsilon_s$  and  $\alpha_0$ , used in the analysis of the experimental data, are provided in Table 1. An example of the two-dimensional distribution of  $\Delta\alpha$  and  $\Delta c_p$  within the jet is shown in Figure 6d. Note that due to the pixel noise remaining after background removal, further data smoothing was required.

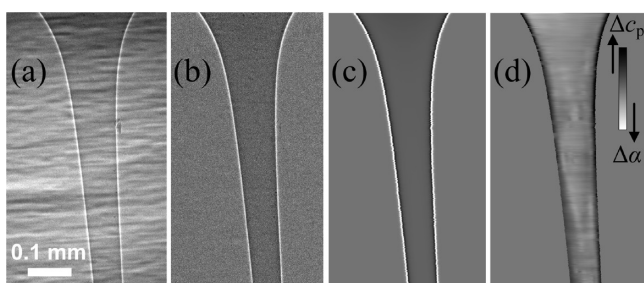


**Figure 6.** Radiation transmission and absorption processing steps. Example based on test 11 (PEO 5%, 2.8 kV/cm, 1.9 mL/h) data. (a) Raw image. (b) Image after background removal and normalization,  $T_{\text{exp}}$ . (c) Wave propagation simulation,  $T_{\text{sim}}$ , assuming a homogeneous jet. (d) Distribution of the absorption coefficient  $\Delta\alpha$  (eq 2) and polymer concentration  $\Delta c_p$  (eq 3) (smoothed). Dark regions denote low absorption and high concentration, while bright regions denote high absorption and low concentration.

### 3. RESULTS AND DISCUSSION

**3.1. Jet Radius.** Jet radius measurements were carried out on electrospinning PEO 3% solutions (tests 2–5), PEO 5% solutions (tests 6–13), a PMMA 15% solution (test 1), and glycerol (test 0). Image examples shown in Figure 7

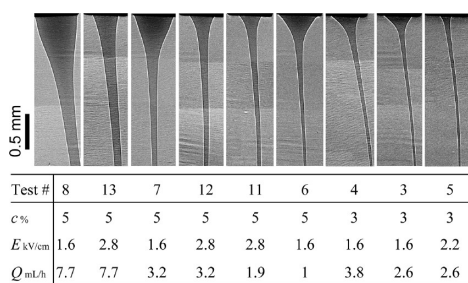


**Figure 7.** Representative test cases of 3% and 5% PEO. The flow in each image was steady state, at test conditions provided in the table. The jet diameter narrows (from left to right) when the electric field is higher and the flow rate and solution concentration are lower.

demonstrate that the jet diameter narrows earlier along the jet when under higher electric fields and lower flow rates and polymer concentrations. Additionally, these process variables influence the opening angle and height of the Taylor cone at the beginning of the jet, as also shown by Reznik et al.<sup>35</sup> and Feng,<sup>36</sup> as well as the degree of wetting of the lower face of the stainless steel needle. The jet radius reduction ratios within up to 8 mm from the jet start ranged between 5 and 24 for the

PEO tests, 10 for the PMMA test, and 31 for the glycerol test. The radius profiles versus the position along the jet are depicted in Figure 8.

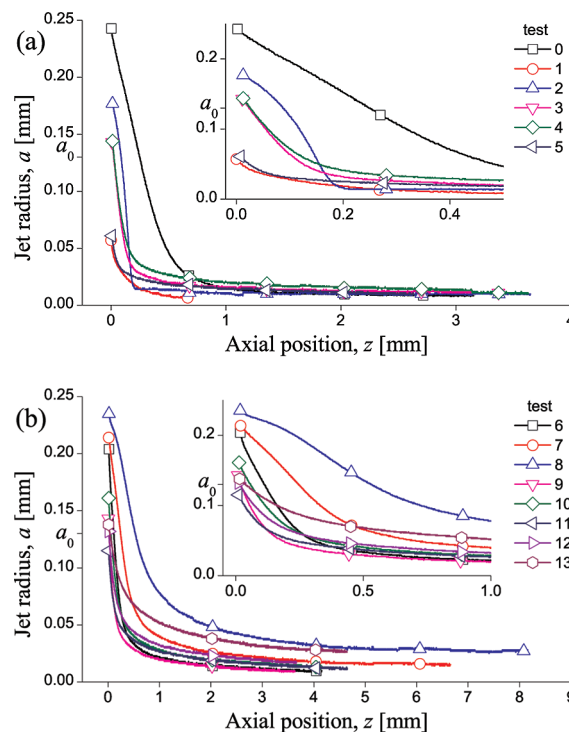


**Figure 8.** Measured jet radius  $a$  at position  $z$  along the jet. The jet profile is measured at 1 pixel resolution ( $0.67 \mu\text{m}$ ), both axially and radially. The insets magnify the early portion of the jet.  $a_0 = 0.13 \text{ mm}$  designates the capillary inner radius. (a) Glycerol (test 0), PMMA 15% (test 1), and PEO 3% (tests 2–5). (b) PEO 5% (tests 6–13).

Analysis of electrically driven fluid jets has shown that the jet reaches an asymptotic regime sufficiently far from the needle orifice. The dimensionless jet radius  $\hat{a}$  can be expressed by a power law of the form  $\hat{a} \sim \hat{z}^{-\beta}$ , where  $\hat{z}$  is the dimensionless distance from the orifice and  $\beta$  is a positive exponent.<sup>37–41</sup> The values of  $\beta$  vary, depending on the fluid type and analysis method. For Newtonian fluids, assuming a negligible viscosity effect, the exponent was estimated as  $\beta = 1/4$ .<sup>37</sup> Using a power-law rheologic constitutive equation, this estimate was generalized to non-Newtonian jets having a flow index  $>2$ , to  $\beta \geq 1/2$ ,<sup>38</sup> which converged to  $\beta = 1/2$  for jets with a high flow index. Other estimates for Newtonian fluids were  $\beta = 1$  (hyperbolic shape), for both viscosity-dominated<sup>40</sup> and capillary-dominated<sup>41</sup> flows. The jet viscoelastic rheology was modeled by Reneker et al. using Maxwell damper-spring elements, providing a complete description of the jet dynamics throughout both the straight and bending-instability regions.<sup>4</sup> Running this model for the jet straight region, we observed a good asymptotic fit to a power law, with  $\beta \cong 1/4$  over a wide range of the dimensionless parameters (voltage, elastic modulus, and electric charge). Solvent evaporation, added to the model by Yarin et al., was shown to have a major effect on the jet radius at the bending-instability region, while only a minor effect at the straight region.<sup>42</sup>

Using the orifice internal radius  $a_0$  as the length scale, the power law takes the form

$$\frac{a}{a_0} = \frac{1}{k} \left( \frac{z}{a_0} \right)^{-\beta} \quad (4)$$

where the dimensionless parameter  $k$  determines the jet radius reduction rate. The radius measurements of all tests can be collapsed onto a common asymptotic curve ( $k = 1$ ), by multiplying each profile displayed in Figure 8, by a suitable value of  $k$ . The results are depicted in Figure 9a and apply when

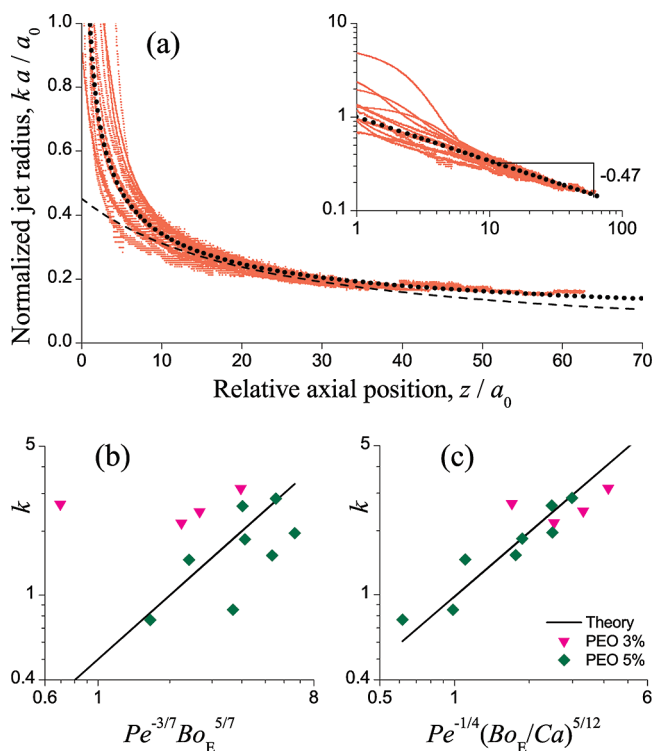


**Figure 9.** Comparison of measured jet radius to theory at distances of  $z/a_0 > 10$  from the orifice. (a) Normalized jet radius  $ka/a_0$  at position  $z/a_0$  along the jet, for the combined data of tests 0–13, where each test set is multiplied by the constant  $k$  pertaining to that test. The power fit (dotted line) corresponds to  $a/a_0 = (z/a_0)^{-0.47}$ , where the exponent is measured in inset graph. The hyperbolic fit (dashed line) corresponds to  $a/a_0 = (z/a_0 + p)^{-1}$ , where  $p = 23.1$ . (b) Measured coefficient  $k$  for tests 2–13 (PEO), compared to the theoretical dimensionless prediction (solid line) for capillary-dominated flow. The predicted value is adjusted by a constant of order 1. (c) As in (b), but for viscosity-dominated flow.

the distance from the orifice,  $z$ , is larger than  $\sim 10$  times the orifice's internal radius,  $a_0$ . The slope of the asymptote was measured as  $\beta = 0.47 \cong 1/2$  (inset in Figure 9a) and compared with a hyperbolic fit.

The parameter  $k$  depends on the flow type. The flow is considered viscosity-dominated when the viscosity, flow rate, and electric field are high, yielding smaller surface tension stresses than viscous and electric stresses. Conversely, the flow is considered capillary-dominated when the surface tension stresses are comparably higher than the viscous and electric stresses. Using dimensionless numbers, theoretical expressions for  $k$  are given by  $k_{\text{vis}} \sim \epsilon_m^{1/6} Pe^{-1/4} (Bo_E/Ca)^{5/12}$  for viscosity-dominated flow,<sup>40</sup> and  $k_{\text{cap}} \sim \epsilon_m^{2/7} Pe^{-3/7} Bo_E^{5/7}$  for capillary-dominated flow,<sup>41</sup> where  $\epsilon_m \cong 1$  is the permeability of the medium (air),  $Pe = 2\nu_0/(\sigma a_0)$  is the Péclet number,  $Bo_E = a_0 E^2/\gamma$  is the electric Bond number, and  $Ca = \mu\nu_0/\gamma$  is the capillary

number.  $\nu_0 = Q/(\pi a_0^2)$  is the jet initial velocity. The dimensional counterparts are the following:  $k_{\text{vis}}^d \sim \epsilon_m^{1/6} a_0^{2/3} \nu_0^{-2/3} \sigma^{1/4} \mu^{-5/12} E^{5/6}$  and  $k_{\text{cap}}^d \sim \epsilon_m^{2/7} a_0^{2/7} \nu_0^{-3/7} \sigma^{3/7} \gamma^{-5/7} E^{10/7}$ . Note that  $k_{\text{vis}}$  is independent of the surface tension  $\gamma$ , while  $k_{\text{cap}}$  is independent of the viscosity  $\mu$ . The measured values of  $k$  were compared with these theoretical predictions, assuming both capillary-dominated (Figure 9b) and viscosity-dominated (Figure 9c) flows. A good fit to the theoretical model was achieved when assuming viscosity-dominated flow.

Reznik et al.<sup>41</sup> provide an additional criterion for determining the flow type, using the dimensionless number  $B = Bo_E Ca / Pe$ , where  $I$  is the overall electric current led by the jet. When  $B \leq 0.01$ , the flow is dominated by capillarity, and when  $B \geq 1$ , the flow is dominated by viscosity. However, when  $0.01 < B < 1$ , both surface tension and viscous stresses influence the jet shape. Based on the data provided in Table 1,  $0.1 < B < 0.9$  for the PEO 3% tests, which is within the interim regime, while  $3 < B < 40$  for the PEO 5% tests, which falls within the viscosity-dominated regime. Thus, we can conclude that the experimental results for the PEO tests are in good agreement with the theoretical models. It should be clarified that this analysis applies to the straight section of the jet, before the onset of bending instability, which introduces a dramatic decrease in jet radius and an increase in jet surface area, causing rapid evaporation.<sup>4,6,7,42–44</sup>

At regions closer to the orifice, namely within the Taylor cone (Figure 10a), viscous stresses are lower and the effect of surface tension becomes more significant, while the effects of flow rate and electric field remain similar to those at the asymptotic region of the jet. We use the dimensionless number  $Bo_E/Pe = (1/2)a_0^2\nu_0^{-1}\sigma\gamma^{-1}E^2$  to express these effects for the

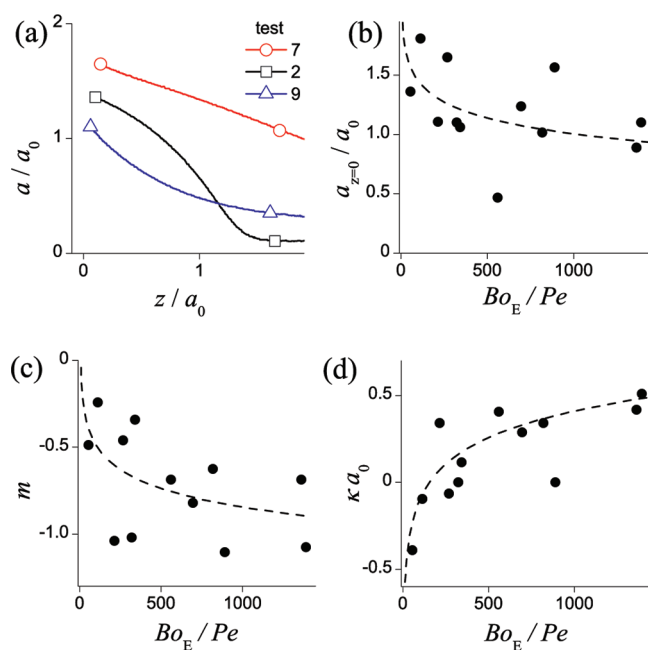


**Figure 10.** Jet radius profile near the orifice and its dependence on the dimensionless number  $Bo_E/Pe$  for tests 2–13 (PEO). (a) Typical cases of the jet radius  $a/a_0$  at position  $z/a_0$  along the jet: straight (test 7: PEO 5%, 1.6 kV/cm, 3.2 mL/h,  $Bo_E/Pe = 267$ ), convex (test 2: PEO 3%, 0.6 kV/cm, 1.9 mL/h,  $Bo_E/Pe = 55$ ), and concave (test 9: PEO 5%, 2 kV/cm, 1 mL/h,  $Bo_E/Pe = 1390$ ). (b) Initial jet radius  $a_{z=0}/a_0$ . (c) Initial jet slope  $m$ . (d) Initial jet curvature  $\kappa a_0$ .

PEO tests (Figure 10). When the electric field was lower and the flow rate and surface tension were higher (smaller  $Bo_E/Pe$ ), the wetting of the needle was larger (Figure 10b), the initial slope of the profile was smaller (Figure 10c), and the curvature of the profile became negative (Figure 10d). In other words, the Taylor cone became larger and convex. On the other hand, when  $Bo_E/Pe > 1000$ , the Taylor cone features tended to converge to the following conditions: no wetting  $a_{z=0} \cong a_0$ , slope  $m = da/dz \cong -1$ , and curvature  $\kappa \cong 1/(2a_0)$ .

The initial semivertical angle of the Taylor cone in these PEO tests varied between  $13^\circ$  and  $48^\circ$ . By comparison, Reznik et al.<sup>35</sup> have experimentally and theoretically shown that at an electric field with  $Bo_E$  above a critical value, jetting sets in, and the jet acquires an almost conical shape with a semivertical angle of  $30^\circ$ , significantly smaller than the  $49.3^\circ$  angle of the Taylor cone.

**3.2. Jet Velocity.** An upper-bound estimate for jet velocity  $v$  (Figure 11a,b) and strain rate  $s$  (velocity gradient) (Figure 11c)

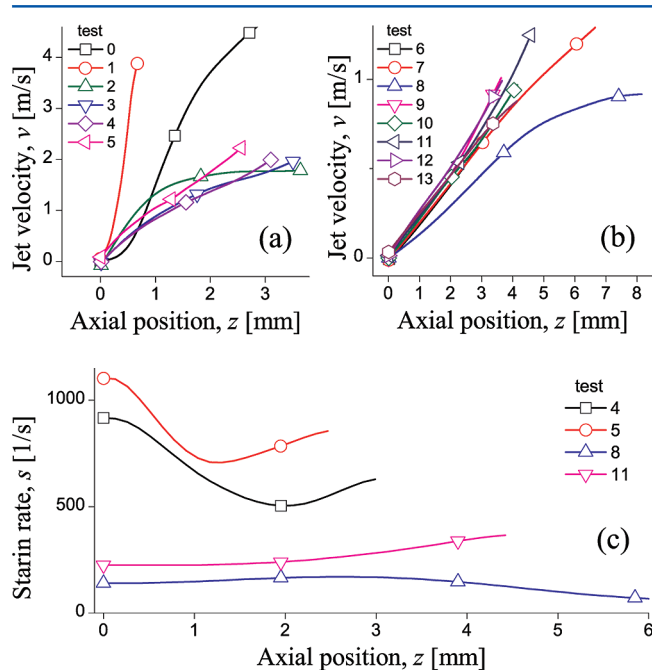


**Figure 11.** Estimated jet velocity  $v = Q/(\pi a^2)$  at position  $z$  along the jet, assuming mass conservation. (a) Glycerol (test 0), PMMA 15% (test 1), and PEO 3% (tests 2–5). (b) PEO 5% (tests 6–13). (c) Examples of strain rate  $s$ .

can be obtained from the radius measurements by assuming mass conservation (i.e., no evaporation), that is,  $v = Q/(\pi a^2)$ , where  $Q$  is the volumetric flow rate. Typical estimated maximal values were  $v \sim 2$  m/s and  $s \sim 1000$  1/s for the PEO 3% tests,  $v \sim 1$  m/s and  $s \sim 200$  1/s for the PEO 5% tests,  $v \sim 4$  m/s and  $s \sim 7000$  1/s for the PMMA 15% test, and  $v \sim 5$  m/s and  $s \sim 2000$  1/s for the glycerol test. Note the nonmonotonic evolution of the strain rate in Figure 11c, which indicates the transition from the capillary-dominated region (Taylor cone) to the viscosity-dominated region.

Using the power law of eq 4, the asymptotic velocity sufficiently far from the orifice can be written as

$$\frac{v}{v_0} = k^2 \left( \frac{z}{a_0} \right)^{2\beta} \cong \frac{k^2 z}{a_0} \quad (5)$$

where, as before,  $\beta = 0.47 \cong 1/2$ . The corresponding dimensionless strain rate  $\hat{s}$  saturates to approximately  $\hat{s} = sa_0/v_0 \cong k^2$ . Thus, for the studied viscosity-dominated test conditions, the jet strain rate, expressed by  $k_{\text{vis}}^2$ , increases with the electric field  $E$  and conductivity  $\sigma$  and decreases with the velocity  $v_0$  (or flow rate  $Q$ ) and viscosity  $\mu$  (or solution concentration  $c$ ). Note that the “grouping” of the graphs in Figure 11 is due to the sensitivity of  $k_{\text{vis}}^2$  to the widely disparate viscosity values between the groups (see Table 1).

Measurements of the jet vertical velocity using particle tracing,  $v_p$ , are presented for PEO 5% tests 14 (4 kV/cm, 2.6 mL/h) and 15 (4 kV/cm, 6.4 mL/h) and are compared to velocity estimation based on the mass conservation assumption,  $v_c$  (Figure 12). The comparison revealed a large deviation

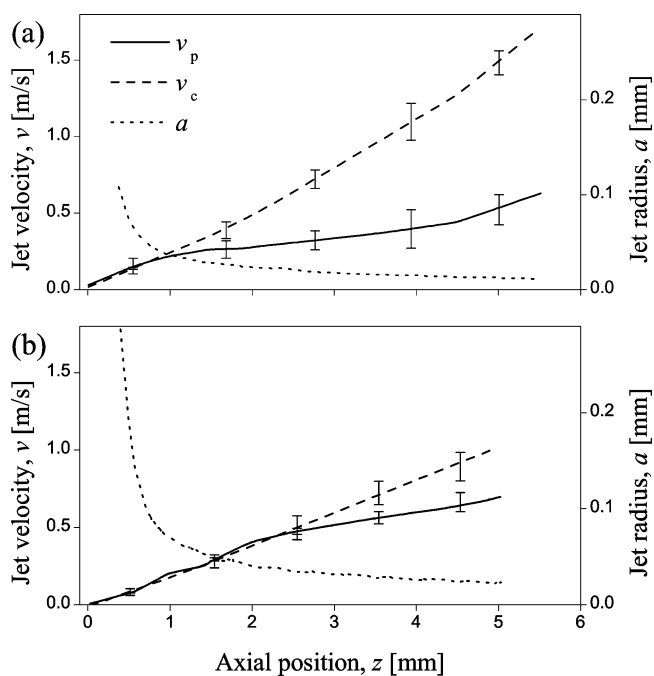


**Figure 12.** Examples of vertical velocity measurements using silica microbeads,  $v_p$ , compared to velocity estimation from the measured radius  $a$  assuming mass conservation,  $v_c$ . Electrospinning of PEO 5%, under an electric field of 4 kV/cm. (a) Test 14: flow rate of 2.6 mL/h, 589 data points. (b) Test 15: flow rate of 6.4 mL/h, 696 data points.

between the two measurement methods, which intensified with the distance from the orifice and was more pronounced at the lower flow rate (Figure 12a). The difference in strain rate is by a factor of  $\sim 2$ .  $v_p$  and  $v_c$  coincide close to the orifice, but they begin to separate at a jet diameter of  $2a \cong 50$   $\mu\text{m}$ , significantly larger than the particle mean size ( $\sim 2$   $\mu\text{m}$ ), thereby ruling out any possibility of adverse effects of the particles on flow. The possible impact of the X-ray beam, especially due to ionization of the air surrounding the jet, can also be ruled out in view of the good correlation between the methods at the beginning of the jet. It also seems unlikely that the dynamic evolution of the polymer network could affect the particles velocity to the extent observed.

Thus, this measurement and comparison suggest a very rapid evaporation, at a distance of only a few millimeters from the jet start. Note that the asymptotic ratio of jet surface area to volume, inversely proportional to the jet radius, is about twice as large in the 2.6 mL/h case compared to the 6.4 mL/h case, accounting for the higher evaporation rate in lower flow rate.

The solvent used in these tests was water, a nonvolatile solvent; however, the relative humidity was fairly low (40%).

The use of particles provides a high-resolution internal view of the flow field within the jet. The image in Figure 13a displays

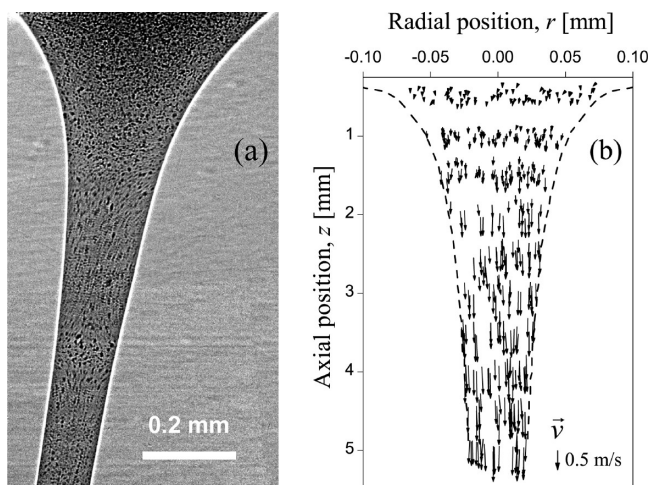


**Figure 13.** Typical flow field during electrospinning of PEO 5% solution in water, mixed with 0.9 vol % silica microbeads, under an electric field of 4 kV/cm and flow rate of 6.4 mL/h (test 15). (a) Two-pulsed X-ray image of a 1 mm long jet section, captured with a 73.6  $\mu$ s time interval between exposures. (b) Velocity vector field,  $\vec{v}$ , generated by particle tracing in a 5 mm long jet section (note the uneven axis scales).

an example of the flow regime during the initial formation of the jet. As seen, flow lines emerge when the velocity is fast enough, and the flow appears to be laminar, as expected from the low Reynolds number. The flow field velocity measurements (Figure 13b) showed a predominantly vertical velocity that seemed to be uniformly distributed across the jet.

However, fitting the data of test 15 (PEO 5%, 4 kV/cm, 6.4 mL/h) to a parabolic shape, as suggested by Reznik et al.,<sup>41</sup> revealed a Poiseuille distribution of the vertical velocity across the jet (Figure 14a), with lower velocity at the jet center when compared to the jet boundary. By contrast, vertical velocity distribution was close to uniform in the lower flow rate case (test 14: PEO 5%, 4 kV/cm, 2.6 mL/h, Figure 14b), possibly

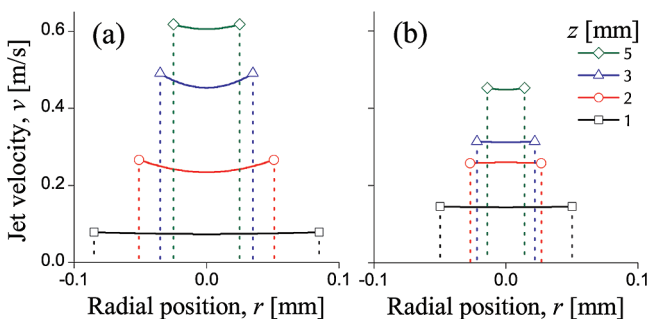


**Figure 14.** Examples of vertical velocity distribution across the jet, at given locations  $z$  along the jet, as a function of the radial distance  $r$  from the jet center. The values were averaged along the X-ray beam path and were obtained by parabolic fitting of the test data. Electrospinning was done for PEO 5% solution in water, mixed with 0.9 vol % silica microbeads, under an electric field of 4 kV/cm. (a) Test 15: flow rate of 6.4 mL/h ( $\bar{R}^2 > 0.95$ ). (b) Test 14: flow rate of 2.6 mL/h ( $\bar{R}^2 > 0.75$ ).

due to the smaller jet radius. The sign of the velocity profile curvature in test 15 was opposite to that predicted by Reznik et al. for a viscosity-dominated flow. This phenomena could be influenced by the nonuniform distribution of the polymer (section 3.3).

**3.3. Polymer Concentration Distribution.** Measurements of X-ray absorption variations within the jet were carried out on PEO 3% solutions (tests 2–5), PEO 5% solutions (tests 6–13), and a PMMA 15% solution (test 1). The resulting concentration variations are attributed to the effects of evaporation and polymer network stretching. In view of the partial correction for scattering effects (eq 2), these results should be regarded as indicating trends.

As concentration variations are expected to assume circular symmetry at a jet cross section, measurement of radiation transmission through the center of a jet should yield the average absorption change of the jet at a given axial position  $z$ . The resulting evolution of the average absorption coefficient,  $\Delta\alpha$ , along the centerline of the jet of several test cases, is shown in Figure 15a. As seen, the absorption coefficient tends to

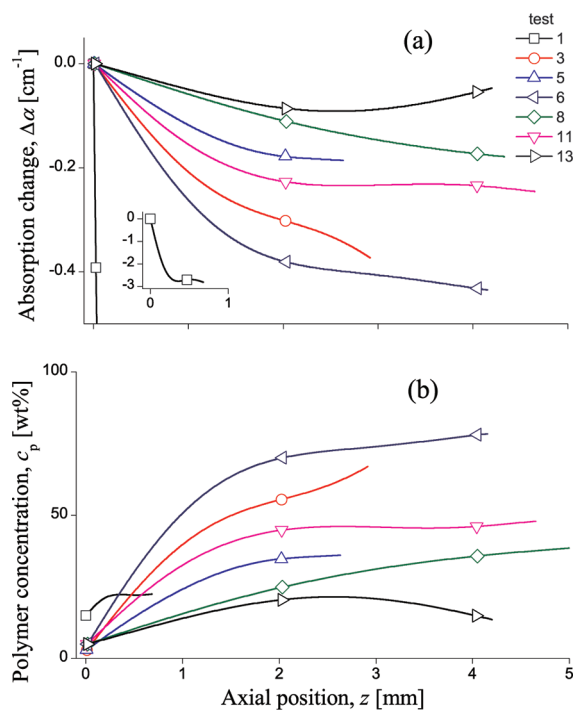


**Figure 15.** Measured average change in X-ray absorption and polymer concentration, in relation to the distance  $z$  from the orifice, based on radiation transmission measurements along the jet centerline. Test 1 is PMMA 15% (inset), tests 3 and 5 are PEO 3%, and tests 6–13 are PEO 5%. (a) Absorption coefficient change,  $\Delta\alpha$ . (b) Polymer concentration,  $c_p$  [wt %].

decrease with the distance from the orifice. At the jet beginning, the rate of decrease is high but slows at increasing distances and sometimes even reverses (e.g., test 13: PEO 5%, 2.8 kV/cm, 7.7 mL/h). Note the high absorption change in test 1 (PMMA 15%, 0.8 kV/cm, 1.9 mL/h, see inset in Figure 15a) due to the high disparity in mass absorption coefficients between PMMA and chloroform.

The polymers in these tests have lower X-ray mass absorption coefficients than their respective solvents (refer to Table 1), and therefore the decrease in the absorption coefficient reflects an increase in polymer concentration (Figure

15b). The results show a significant rise in concentration within the first few millimeters from the jet start, indicating substantial mass loss due to evaporation. This observation supports the similar finding obtained from the velocity measurements in section 3.2. The slowing down, and even reversal, of the concentration change rate along the jet may imply an onset of additional mechanisms, such as polymer chains disentanglement or skin solidification, which retards evaporation rates. Further evaporation may leave voids in the jet core and allow partial relaxation of the polymer matrix.<sup>11</sup>

A common behavior emerges when examining the polymer relative concentration change,  $\Delta c_p/c$ , recorded in tests 3–12 (PEO in water), as a function of the relative jet radius,  $a/a_0$  (Figure 16). A steep rise in polymer concentration was

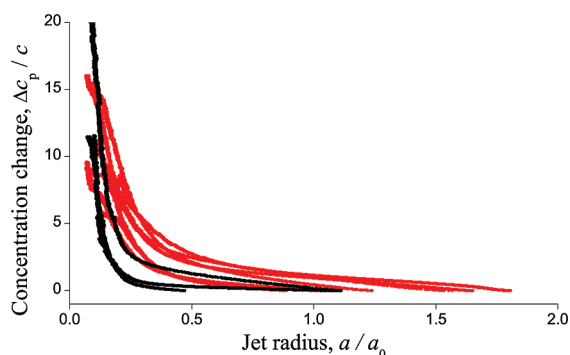


**Figure 16.** Relative concentration change  $\Delta c_p/c$  vs relative jet radius  $a/a_0$ , derived from the X-ray absorption measurements at jet center of tests 3–5 (PEO 3%, black lines) and tests 6–12 (PEO 5%, red lines).

observed at  $a/a_0 \cong 0.2$ , marking a critical radius of  $\sim 25 \mu\text{m}$ , below which rapid evaporation is initiated. Interestingly, velocity measurements demonstrated a similar value, marking the radius at which rapid evaporation began (Figure 12). As noted by Yarin et al.,<sup>42</sup> rapid evaporation starts upon rapid increase in the ratio of the jet surface area to volume, which is inversely proportional to the jet radius.

The concentration change rate can be estimated from the slope of the plot in Figure 16 in the asymptotic region, using the power dependence

$$\frac{\Delta c_p}{c} \sim \left(\frac{a}{a_0}\right)^{-\phi} \quad (6)$$

where the measured exponent is  $\phi \cong 2 \pm 0.5$  for PEO tests 3–12. Since this concentration change is due to evaporation, the corresponding local mass loss rate is then  $\sim c(a/a_0)^{-2}$  in the measured region or, in other words, inversely proportional to the jet cross-sectional area.

Absorption measurements across the jet at different axial positions (Figure 17) revealed nonuniform distribution of the polymer, with high concentration boundary layer formed as a result of evaporation. In addition, a peak emerged at the jet center, starting at cross sections  $z \geq 1 \text{ mm}$  from the orifice. Our previous theoretical and experimental study<sup>11</sup> attributed this rise to polymer network stretching during electrospinning, which causes lateral contraction of the network, thereby increasing polymer concentration at the center. Polymer chains entangled in a network were shown to approach full extension when the jet vertical velocity was approximately  $v/v_0 \cong N_s^{1-\nu}$ , where  $N_s$  is the number of monomers in a subchain (a section

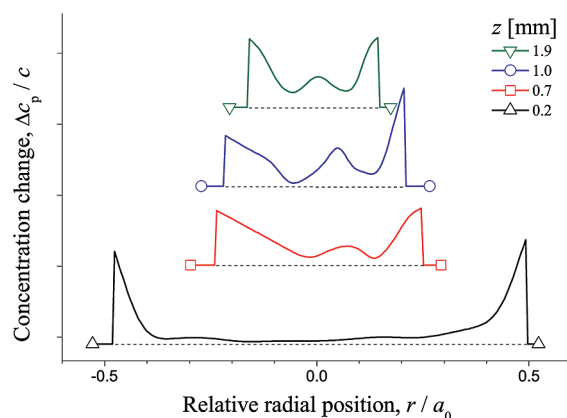


**Figure 17.** Typical polymer relative concentration change across the jet,  $\Delta c_p/c$ , vs the relative radial distance from the jet center,  $r/a_0$ , for several axial positions  $z$  along the jet. The data are derived from the X-ray absorption measurements of PEO 5%, under an electric field of 2.8 kV/cm and flow rate of 1.9 mL/h (test 11). The dashed horizontal lines represent zero concentration change,  $\Delta c_p/c = 0$ , corresponding to a homogeneous jet with uniform concentration  $c_p = c$ .

of a polymer chain between two adjacent entanglement nodes) and  $\nu$  is Flory's exponent. Considering a PEO 5% solution, this criterion predicts significant stretching at a relative radius of  $a/a_0 \cong 0.4$ , which occurs close to the jet start, in good agreement with the result observed in Figure 17.

Evaporation and stretching impart contradicting effects on the polymer concentration distribution. Evaporation tends to increase concentration at the jet boundary, while stretching leads to its increase at the jet center. Fast stretching of the solution jet counteracts polymer network relaxation due to evaporation and skin formation and causes lateral inward contraction of the network. Material properties and electrospinning conditions influence the relative impact of stretching and evaporation on the polymer matrix and eventually determine the resulting macrostructure of nanofibers (see examples of homogeneous and porous structures in Greenfield et al.<sup>11</sup>).

The balance between these two processes is demonstrated in Figure 18, which compares the concentration along the jet centerline to that along an offset of half-radius ( $a/2$ ) from the centerline. The comparison is done within the same solution (PEO 5% in water) to avoid concentration effects on evaporation. Under an electric field of 2.8 kV/cm and flow rate of 1.9 mL/h (test 11, Figure 18a), the concentration at the center was higher than at the offset, for sufficiently small jet relative radius  $a/a_0$ , indicating noticeable stretching. When reducing the electric field to 2 kV/cm and leaving the flow rate unchanged (test 10, Figure 18b), the concentrations at the center and at the offset remained similar, evidence for balanced effects of evaporation and stretching on polymer distribution at the jet core. Finally, when leaving the electric field unchanged (as in test 11) and increasing the flow rate to 7.9 mL/h (test 13, Figure 18c), a higher concentration was observed at the offset than at the center, evidence for dominant evaporation.

Similar behavior was observed when testing PEO 3%. For example, test 5 (2.2 kV/cm, 2.6 mL/h) involved higher electric field and lower flow rate than test 4 (1.6 kV/cm, 3.8 mL/h) and yielded higher concentrations at the center when compared to the offset. These trends are in agreement with the theoretical prediction,<sup>11</sup> which has shown that the local axial stretching of polymer chains, and consequently their lateral contraction, are

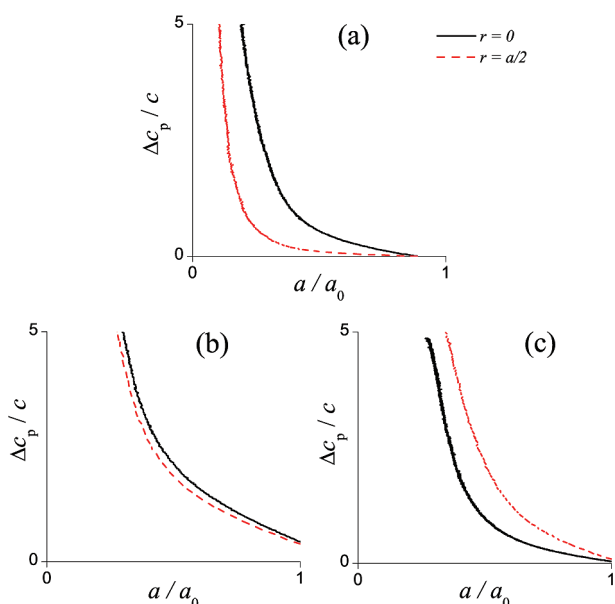


**Figure 18.** Comparison of the relative concentration change  $\Delta c_p/c$  at the jet center ( $r = 0$ ) to that measured at a radial offset from the center ( $r = a/2$ , averaged over the range  $0.4a$  to  $0.6a$ ), presented vs the relative jet radius  $a/a_0$ . The data were derived from the X-ray absorption measurements of PEO 5% in (a) test 11 (2.8 kV/cm, 1.9 mL/h), (b) test 10 (2 kV/cm, 1.9 mL/h), and (c) test 13 (2.8 kV/cm, 7.9 mL/h).

proportional to the jet relative local velocity  $v/v_0$ , and hence, in view of eq 5), are proportional to  $k_{\text{vis}}^2$ . Regardless of these findings, it should be noted that high concentration at the jet boundary was observed in all tests.

#### 4. CONCLUSIONS

Fast X-ray phase-contrast imaging was applied for high-resolution investigation of the initial straight section of electrospinning polymer jets, extending up to 10 mm from the orifice. The experiment aimed at providing data on the flow field and polymer concentration distribution within the jet, which can help describe the state of the polymer network during electrospinning.

Details relating to jet radius, velocity, and strain rate were measured for a range of electrospinning conditions and polymer solutions. Particle tracing velocimetry allowed for flow regime viewing inside the jet, characterized by laminar flow and dominant vertical velocity. The velocity was found to be slower than an estimation based on mass conservation assumption, indicating a substantial mass loss due to evaporation at a very early stage of the process.

Measurement of pixel intensities were converted to X-ray radiation absorption coefficients that allowed for estimation of the polymer distribution within the jet. Concentrations were found to rapidly increase below a critical radius, evidence of rapid evaporation. The rate of mass loss due to evaporation seemed to be much higher than theoretical predictions.<sup>42</sup> In addition, the concentration variation across the jet revealed high concentrations at the jet boundary due to evaporation as well as a concentration rise at the jet center. The latter phenomenon is attributed to polymer stretching that causes lateral contraction of the polymer network toward the jet center and is in good agreement with theoretical models.<sup>11</sup> Moreover, it was shown that evaporation is dominant when stretching is

weaker (e.g., at lower electric field and/or higher flow rate), canceling the concentration peaks measured at the jet center.

The balance between the effects of evaporation and stretching determines the polymer network nonequilibrium conformation during electrospinning and can help clarify the reasons for the diverse macrostructures and properties found in solid nanofibers. In particular, the size-dependent mechanical, thermomechanical, and thermodynamic properties of as-spun nanofibers,<sup>8,9,12,45</sup> such as the rise of the elastic modulus at small diameters, are attributed to the internal molecular and supermolecular structure of the polymer matrix in nanofibers.<sup>11</sup>

X-ray imaging during electrospinning can provide internal flow and concentration data, unattainable by other in-situ measurement methods. The current implementation of the method is, however, limited to the initial section of the jet that is sufficiently stable to be captured within the small field of view of the imaging system. Nevertheless, further investigation downstream, at narrower jet diameters on the order of micrometers, can provide evidence for polymer chains disentanglement and reveal nonuniform flow regime due to rapid evaporation, possibly with streamlines toward the jet boundary. Such observations may be important for electrospinning applications such as drug delivery and coatings.

#### ■ AUTHOR INFORMATION

##### Corresponding Author

\*Tel 972 4 957 1287; fax 972 4 957 1291; e-mail green\_is@netvision.net.il.

##### Notes

The authors declare no competing financial interest.

#### ■ ACKNOWLEDGMENTS

We gratefully acknowledge the financial support of the United States–Israel Binational Science Foundation (BSF Grant 2006061), the RBNI–Russell Berrie Nanotechnology Institute, and the Israel Science Foundation (ISF Grant 770/11). Use of the Advanced Photon Source, an Office of Science User Facility operated for the U.S. Department of Energy (DOE) Office of Science by Argonne National Laboratory, was supported by the U.S. DOE under Contract DE-AC02-06CH11357. We acknowledge Dr. Arkadii Arinstein for insightful discussions on polymer dynamics. We thank Dr. Rene Van-Hout for valuable advice on X-ray image processing.

#### ■ REFERENCES

- (1) Han, T.; Yarin, A. L.; Reneker, D. H. *Polymer* **2008**, *49* (6), 1651–1658.
- (2) Gupta, P.; Elkins, C.; Long, T. E.; Wilkes, G. L. *Polymer* **2005**, *46* (13), 4799–4810.
- (3) Reneker, D. H.; Yarin, A. L.; Zussman, E.; Xu, H. *Adv. Appl. Mech.* **2007**, *41*, 43–195.
- (4) Reneker, D. H.; Yarin, A. L.; Fong, H.; Koombhongse, S. *J. Appl. Phys.* **2000**, *87* (9), 4531–4547.
- (5) Bellan, L. M.; Craighead, H. G.; Hinstroza, J. P. *J. Appl. Phys.* **2007**, *102* (9), 094308.
- (6) Hohman, M. M.; Shin, M.; Rutledge, G.; Brenner, M. P. *Phys. Fluids* **2001**, *13* (8), 2201–2220.
- (7) Shin, Y. M.; Hohman, M. M.; Brenner, M. P.; Rutledge, G. C. *Polymer* **2001**, *42* (25), 9955–9967.
- (8) Burman, M.; Arinstein, A.; Zussman, E. *Appl. Phys. Lett.* **2008**, *93* (19), 193118.
- (9) Arinstein, A.; Burman, M.; Gendelman, O.; Zussman, E. *Nat. Nanotechnol.* **2007**, *2* (1), 59–62.

- (10) Burman, M.; Arinstein, A.; Zussman, E. *Europhys. Lett.* **2011**, *96*, 16006.
- (11) Greenfeld, I.; Arinstein, A.; Fezzaa, K.; Rafailovich, M. H.; Zussman, E. *Phys. Rev. E* **2011**, *84* (4), 041806.
- (12) Zussman, E.; Arinstein, A. *J. Polym. Sci., Part B: Polym. Phys.* **2011**, *49* (10), 691–707.
- (13) Guenther, A. J.; Khombhongse, S.; Liu, W. X.; Dayal, P.; Reneker, D. H.; Kyu, T. *Macromol. Theory Simul.* **2006**, *15* (1), 87–93.
- (14) Dayal, P.; Kyu, T. *Phys. Fluids* **2007**, *19* (10), 107106.
- (15) Dayal, P.; Liu, J.; Kumar, S.; Kyu, T. *Macromolecules* **2007**, *40* (21), 7689–7694.
- (16) Koombhongse, S.; Liu, W. X.; Reneker, D. H. *J. Polym. Sci., Part B: Polym. Phys.* **2001**, *39* (21), 2598–2606.
- (17) Casper, C. L.; Stephens, J. S.; Tassi, N. G.; Chase, D. B.; Rabolt, J. F. *Macromolecules* **2004**, *37* (2), 573–578.
- (18) Deitzel, J. M.; Krauthauser, C.; Harris, D.; Pergantis, C.; Kleinmeyer, J. *Polym. Nanofibers* **2006**, *918*, 56–73.
- (19) Larrondo, L.; Manley, R. S. J. *J. Polym. Sci., Part B: Polym. Phys.* **1981**, *19* (6), 921–932.
- (20) Stephens, J. S.; Frisk, S.; Megelski, S.; Rabolt, J. F.; Chase, D. B. *Appl. Spectrosc.* **2001**, *55* (10), 1287–1290.
- (21) Priebe, M.; Kalbfleisch, S.; Tolkiehn, M.; Koster, S.; Abel, B.; Davies, R. J.; Salditt, T. *New J. Phys.* **2010**, *12*, 1–12.
- (22) MacPhee, A. G.; Tate, M. W.; Powell, C. F.; Yue, Y.; Renzi, M. J.; Ercan, A.; Narayanan, S.; Fontes, E.; Walther, J.; Schaller, J.; Gruner, S. M.; Wang, J. *Science* **2002**, *295* (5558), 1261–1263.
- (23) Wang, Y. J.; Liu, X.; Im, K. S.; Lee, W. K.; Wang, J.; Fezzaa, K.; Hung, D. L. S.; Winkelman, J. R. *Nat. Phys.* **2008**, *4* (4), 305–309.
- (24) Im, K. S.; Fezzaa, K.; Wang, Y. J.; Liu, X.; Wang, J.; Lai, M. C. *Appl. Phys. Lett.* **2007**, *90* (9), 091919.
- (25) Sasov, A. *European Conference for Non-Destructive Testing (ECNDT) 2006, We.1.5.4*, 1–6.
- (26) Richter, A. G.; Guico, R.; Shull, K.; Wang, J. *Macromolecules* **2006**, *39* (4), 1545–1553.
- (27) Gullikson, E. X-Ray Interactions with Matter. [http://henke.lbl.gov/optical\\_constants/](http://henke.lbl.gov/optical_constants/).
- (28) [www.surface-tension.de](http://www.surface-tension.de). Surface tension values of some common test liquids.
- (29) <http://www.smartmeasurement.com>. Conductivity of common fluids.
- (30) Theron, S. A.; Zussman, E.; Yarin, A. L. *Polymer* **2004**, *45* (6), 2017–2030.
- (31) Thomas, D. G. *J. Colloid Sci.* **1965**, *20* (3), 267–277.
- (32) Staben, M. E.; Davis, R. H. *Int. J. Multiphase Flow* **2005**, *31* (5), 529–547.
- (33) Roe, R. J., *Methods of X-ray and Neutron Scattering in Polymer Science*; Oxford University Press: New York, 2000; p xiv, 331 p.
- (34) Reeves, R. V.; White, J. D. E.; Dufresne, E. M.; Fezzaa, K.; Son, S. F.; Varma, A.; Mukasyan, A. S. *Phys. Rev. B* **2009**, *80* (22), 224103.
- (35) Reznik, S. N.; Yarin, A. L.; Theron, A.; Zussman, E. *J. Fluid Mech.* **2004**, *516*, 349–377.
- (36) Feng, J. J. *Phys. Fluids* **2002**, *14* (11), 3912–3926.
- (37) Kirichenko, V. N.; Petrianovsokolov, I. V.; Suprun, N. N.; Shutov, A. A. *Dokl. Akad. Nauk SSSR* **1986**, *289* (4), 817–820.
- (38) Spivak, A. F.; Dzenis, Y. A. *Appl. Phys. Lett.* **1998**, *73* (21), 3067–3069.
- (39) Hohman, M. M.; Shin, M.; Rutledge, G.; Brenner, M. P. *Phys. Fluids* **2001**, *13* (8), 2221–2236.
- (40) Higuera, F. J. *J. Fluid Mech.* **2006**, *558*, 143–152.
- (41) Reznik, S. N.; Zussman, E. *Phys. Rev. E* **2010**, *81* (2), 026313.
- (42) Yarin, A. L.; Koombhongse, S.; Reneker, D. H. *J. Appl. Phys.* **2001**, *89* (5), 3018–3026.
- (43) Thompson, C. J.; Chase, G. G.; Yarin, A. L.; Reneker, D. H. *Polymer* **2007**, *48* (23), 6913–6922.
- (44) Fridrikh, S. V.; Yu, J. H.; Brenner, M. P.; Rutledge, G. C. *Phys. Rev. Lett.* **2003**, *90* (14), 144502.
- (45) Ji, Y.; Li, C.; Wang, G.; Koo, J.; Ge, S.; Li, B.; Jiang, J.; Herzberg, B.; Klein, T.; Chen, S.; Sokolov, J. C.; Rafailovich, M. H. *EPL* **2008**, *84* (5), 56002.